Conducting-Coil Assembly for Producing Three-Dimensional Magnetic Null Points

D. L. Chesny[1,2,*] and N. B. Orange[1,2,3]

[1] *OrangeWave Innovative Science, LLC, Moncks Corner, South Carolina 29461-6808, USA*
[2] *SpaceWave, LLC, Satellite Beach, Florida 32901, USA*
[3] *Etelman Observatory, St. Thomas, U.S. Virgin Islands 00802, USA*

(Received 27 September 2019; revised manuscript received 24 January 2020; accepted 8 May 2020; published 8 June 2020)

Three-dimensional magnetic null points (3D nulls) are sites of dynamic activity and particle acceleration in astrophysical environments. Future laboratory infrastructures to validate theoretical models of observed plasma dynamics about 3D nulls will benefit from an experimental infrastructure that closely reproduces these analytical potential magnetic fields. As such, a conducting-coil assembly is presented that closely matches the theoretical form of a 3D null within an interior volume. Exact magnetic field solutions are attained for a spherical aggregation of circular current-carrying coils with finite cross sections that create a central magnetic null point of vanishing magnetic energy density. This configuration is shown to replicate the fan-plane–spine-axis topology of 3D nulls to a high order within the central volume close to the null. Finally, numerical analyses demonstrate that the investigated architecture is scalable over wide size and energy ranges. Applications of the presented conducting-coil assembly include sophisticated next-generation plasma experiments and particle accelerators.

DOI: 10.1103/PhysRevApplied.13.064019

I. INTRODUCTION

Magnetic null points are sites of dynamic phenomena and particle acceleration in astrophysical plasmas [1–4]. Laboratory studies of these dynamics are achieved largely as a byproduct in tokamak experiments [5,6] but are also the subject of dedicated experiments, mainly on magnetic reconnection [7–10]. As a general description of the conducting-coil infrastructure leading to the production of a magnetic null point, many experiments use a variation of a Helmholtz-coil configuration, where two circular coils, offset by a distance on the order of their radii, are aligned axially with current flow equal in magnitude but opposite in direction [11–15].

As laboratory plasma infrastructures move toward next-generation architectures [16,17], there will be a need for magnetic field topologies that explicitly follow the fan-spine geometry of a three-dimensional magnetic null point (Fig. 1); hereafter 3D nulls. These 3D nulls are characterized by a central magnetic null point where the magnetic flux density vanishes, a two-dimensional (2D) fan plane of field lines directed radially away from the null, and a one-dimensional (1D) spine axis of collimated field lines, perpendicular to the fan plane and also directed away from the null. Such 3D null-point geometries have been used as the background potential magnetic field in robust simulations of torsional modes of magnetic reconnection [18–28]. The first step in transitioning from simulations of torsional reconnection to an experimental architecture for studying its plasma dynamics in a laboratory setting is to construct a conducting-coil assembly that closely matches the mathematical structure of the background 3D nulls. Fortunately, there is a significant amount of theoretical work on the mathematical formulation of 3D nulls [29–31] for use as an analytical guide to their construction.

Conducting-coil production technologies exist that can match the required magnetic field of the user [32,33]. While a widespread function of these coil assemblies is to produce multipole structures, they are engineered for specific applications, including particle accelerators [34]. Here, we analyze the architecture of a unique aggregation of circular conducting coils that closely approximates the mathematical 3D null formulation [30]. We present a test case and match the resulting magnetic field topology to that of a specific theoretical form. We calculate statistical deviations between the experimental and theoretical fields as well as presenting an empirical assessment of its scalability. Possible augmentations to increase the accuracy of the coil assembly are also discussed.

*orangewavedc@gmail.com

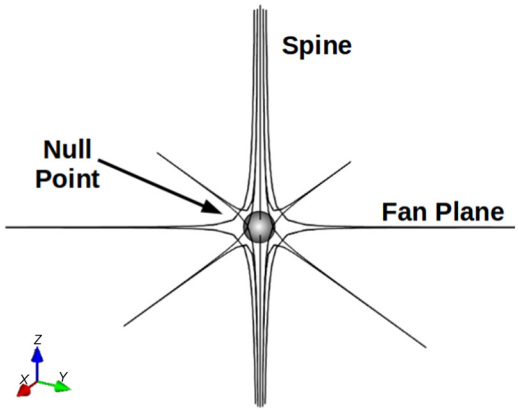

FIG. 1. The magnetic field streamlines of a 3D radial null point. At the central null point ($|\vec{B}| = 0$ T), a 1D "spine" axis of collimated magnetic field lines intersects a 2D "fan plane" of radially pointing magnetic field lines.

II. CONDUCTING-COIL ASSEMBLY AND FORMULATION

A. 3D magnetic nulls

A generalized topological model of 3D magnetic null points [29,30] has quantified a first-order approximation of the magnetic field **B**, expressed as

$$\mathbf{B} = \mathbf{M} \cdot \mathbf{r}, \tag{1}$$

where **M** is a 3×3 magnetization tensor [30] with entries $\partial\mathbf{B}/\partial\mathbf{r}$ and **r** is the position vector $(x, y, z)^T$. The **M** tensor defines all of the physical characteristics of the magnetic field and can be expressed using the four free parameters p, q, $j_\parallel$, and $j_\perp$. The 3D magnetic-null-point field in Cartesian coordinates $[x, y, z]$ is of the form

$$\mathbf{B} = \frac{B_0}{L}\left[x + \frac{1}{2}(q - j_\parallel)y, \frac{1}{2}(q + j_\parallel)x + py, j_\perp y - (p+1)z\right], \tag{2}$$

where B_0 and L are the characteristic magnetic field strength and length, respectively. With this choice of scaling, the magnitude of **B** is approximately equal to B_0 at a linear distance L from the central null in the x-y plane. The fan is in the x-y plane and the spine is aligned with the z axis. The parameters p and q govern the potential part of the field, whereas $j_\parallel$ and $j_\perp$ control the nonpotential behavior of the field and deform field lines as parallel and perpendicular components of the current, respectively. For the simplest form of a radial 3D null as in Fig. 1, where all fan-plane field lines disperse symmetrically out from the null, we choose to set the four free parameters as $p = 1$ and $q = j_\parallel = j_\perp = 0$. For $p > 1$ and $q > 0$, the fan-plane field lines are asymmetric and $j_\parallel, j_\perp \neq 0$ act as currents parallel and perpendicular to the spine axis, respectively, to create a field-line twist in the fan plane. Thus, the final form of the theoretical 3D null-point field that we aim to match is of the form

$$\mathbf{B} = \frac{B_0}{L}[x, y, -2z]\,. \tag{3}$$

This is the precise form of the background potential 3D null-point field in investigations of torsional magnetic reconnection [21,26–28,35]. One can see from Eq. (3) that the choice of sign for the parameter B_0 will force the field lines to either point in along the spine and out along the fan (positive null) or in along the fan and out along the spine (negative null). We aim to construct a conducting-coil assembly that most closely forms both the fan-spine topology and the magnetic flux densities throughout the volume of interest. Additionally, we will show that the choice of current direction will allow switching between the positive and negative forms of the 3D null-point topology.

B. Geometry

A reversed-Helmholtz-coil configuration of two circular conducting coils will form a general magnetic null point along the central axis [16]. However, any semblance of antiparallel collimated spine field lines along this central axis, as in Fig. 1, will quickly diverge, since there are no source currents to sustain them away from the null. To overcome this shortcoming and form a structured fan-spine topology, we exploit azimuthal symmetry by simulating the magnetic field produced by a unique configuration of numerous axially aligned circular conducting coils. As a first-order investigation of the formation of a 3D null point of the form in Fig. 1, we consider a spherical aggregation of circular coils, evenly distributed along the central axis z according to the geometry of the radial null point in Fig. 1 and Eq. (3), with each coil radius descending away from the central null. This configuration is akin to lines of latitude on a sphere. We consider a spherical configuration over other generalized geometries, such as a solenoid or cone, for two reasons. First, we will assume a constant current magnitude in each coil, for simplicity. This dissuades us from the use of a solenoidal configuration, since that will form a constant magnetic field strength along the spine axis, inconsistent with Eq. (3). Second, the magnetic field must increase along the spine axis while allowing maximum access to the volume containing the 3D null. As such, we consider a spherical assembly, while still recognizing that many other geometrical configurations likely exist for forming pure 3D nulls. Fortunately, the results of our analyses in Sec. III will show that although the coil geometry we explore here does induce a deviation from the theoretical away from the null, these errors are symmetric and kept to a minimum throughout the volume due to the spherically symmetric formation of the 3D null. The formulation

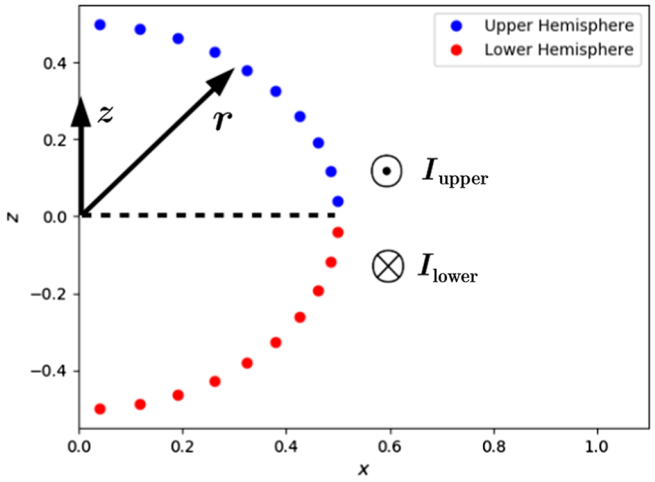

FIG. 2. The geometrical setup of the conducting-coil assembly. Individual coil radii (x-y plane) and z positions are solved on a circle of radius $|\vec{r}|$. The semicircle shown represents a coil assembly of 20 coils in total, with each of the ten coils in the upper hemisphere (blue circles) carrying current I_{upper} and each of the ten coils in the lower hemisphere (red circles) carrying current I_{lower}. Currents I_{upper} and I_{lower} are equal in magnitude but opposite in direction, with respect to the $\hat{k}$ direction.

in this paper provides a framework by which other authors can build and diagnose other forms of 3D nulls.

To mathematically construct this spherical aggregation, we solve for a quarter circle of $2N$ points in the x-z plane, where N is the desired number of coils per hemisphere. The odd-numbered positions of this quarter circle give the horizontal x-coordinate (radius) and vertical z-coordinate (center height) positions for each of N coils. The choice of the odd-numbered positions ensures that no coil lies in the x-y plane forming the fan plane or has a zero radius on the z axis. These coordinates are then mirrored in the negative z direction to form the complete set of radial and height parameters for the spherical aggregation. Figure 2 shows the geometry resulting from this algorithm.

To produce a central magnetic null point, each coil in each corresponding hemisphere will be given equal and opposite current. In the formulation presented here, looking down along the $+z$ axis, each coil in the upper hemisphere has clockwise current I, whereas each coil in the lower hemisphere has counterclockwise current I (Fig. 2). This sets the constraint of a positive 3D null point ($B_0 > 0$), where the magnetic-field-line vectors point out along the fan plane away from the null and in along the spine axis, toward the null. Switching the current directions will produce a negative 3D null ($B_0 < 0$), without loss of generality. A sphere of radius 0.5 m with 20 coils in total, ten per hemisphere, is taken as a test case. The size of this sphere is chosen due to its suitability to a feasible laboratory environment. The effect of an aggregation of a greater or fewer number of coils, or larger and smaller sphere radii, will be discussed in Sec. III.

C. Magnetic field calculations

From this geometry, each circular coil is taken to have a finite cross section (a torus) and be made of copper (Fig. 3). In our code formulation, this choice of material is arbitrary and relies only on a user-supplied engineering current density and material mass density to construct each finite-sized coil torus. The choice of copper is made for the present investigation due to its common use in laboratory coil configurations, but the coils can just as easily be made of other conducting or superconducting [12,33,34] material. Thus, the only constraints to forming the coil tori are the magnitude of current I, the material mass density ρ, and the engineering current density J_e. Table I lists the cross-section radii calculated for the $I = 100$ A test case, plus each of the other three current values investigated in the scalability analysis in Sec. III C (200, 300, and 400 A). Cross-section radii are given to an accuracy of 10^{-2} mm, corresponding to engineering specifications on the order of thousandths of an inch. Further engineering considerations of this finite cross section will be discussed in Sec. IV.

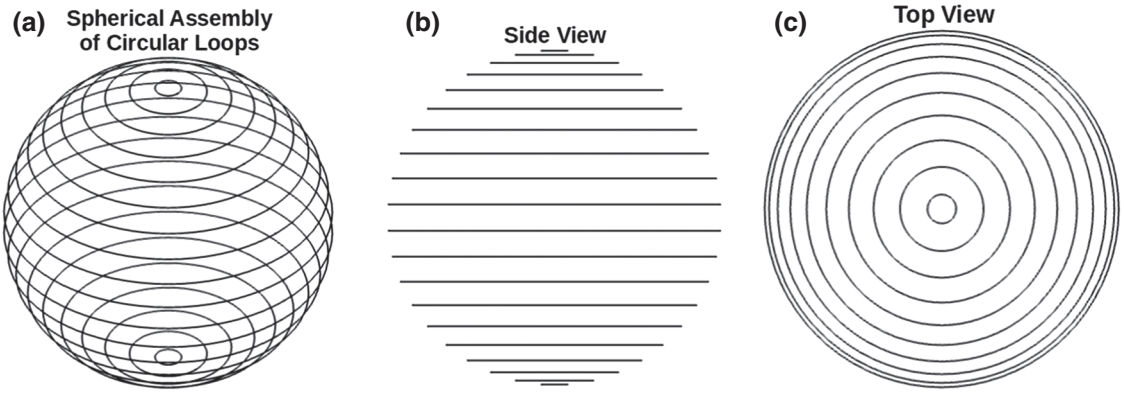

FIG. 3. The computer-aided design (CAD) of the circular coils from the geometry determined in Fig. 2. An aggregation of 20 coils in total forms a spherical configuration. Each coil is represented as a copper torus with a finite cross-section radius.

TABLE I. Copper coil parameters: $\rho = 8.96\ \mathrm{g\,cm^{-3}}$ and $J_e = 500\ \mathrm{A\,cm^{-2}}$.

Current, I (A)	Cross-section radius, r_{cs} (mm)
100	2.52
200	3.57
300	4.37
400	5.05

Calculations of the inner 20 cm × 20 cm magnetic field (400 $\mathrm{cm^2}$), centered on the null, are made at a resolution of 1 cm per pixel for vector presentations (Fig. 6) and a resolution of 0.25 cm per pixel for percent-difference and angle-offset presentations (Figs. 7 top row, 8, and 10). Calculations of the inner 10cm × 10cm percent differences (100 $\mathrm{cm^2}$; Fig. 7, bottom row) are at a pixel resolution of 0.125 cm per pixel. Volumetric calculations of the magnetic field in Fig. 5 (2.5 cm per pixel) and the analysis of Fig. 9 (1.25 cm per pixel) are carried out at resolutions sufficient to accurately represent the presented analyses.

The magnetic field produced by each coil of current I is calculated and superimposed at all pixels to obtain the full field. The expressions below provide simple closed-form analytical expressions for the magnetic field of a current coil that are exact everywhere in space outside the conductor [36], corresponding to the space outside the finite tori with radii in Table I. The magnetic field components for each coil at any point in Cartesian space depend on the current I, the coil radius a, the spherical radial distance $r^2 = x^2 + y^2 + z^2$, and the cylindrical radial distance $\rho^2 = x^2 + y^2$, according to

$$B_x = \frac{Cxz}{2\alpha^2\beta\rho^2}\left[(a^2 + r^2)E(k^2) - \alpha^2 K(k^2)\right], \quad (4)$$

$$B_y = \frac{Cyz}{2\alpha^2\beta\rho^2}\left[(a^2 + r^2)E(k^2) - \alpha^2 K(k^2)\right], \quad (5)$$

and

$$B_z = \frac{C}{2\alpha^2\beta}\left[(a^2 - r^2)E(k^2) + \alpha^2 K(k^2)\right], \quad (6)$$

where $C = \mu_0 I/\pi$, $\alpha^2 = a^2 + r^2 - 2\alpha\rho$, $\beta^2 = a^2 + r^2 + 2\alpha\rho$, and $K(k^2)$ and $E(k^2)$ are the elliptic integrals of the first and second kind, respectively, with argument $k^2 = 1 - \alpha^2/\beta^2$. All elliptic integrals are calculated using the standard SciPy packages SCIPY.SPECIAL.ELLIPK and SCIPY.SPECIAL.ELLIPE. The constant $\mu_0 = 4\pi \times 10^{-7}\ \mathrm{N/A^2}$ is the permeability of free space.

D. Relaxation method

To minimize the differences in magnetic field strength between the theoretical 3D null formulation and the conducting-coil assembly, we implement a custom semisupervised relaxation method. This routine constrains the theoretical value of B_0 to most closely reproduce the defined test case of a 0.5-m radius spherical assembly with a total of 20 copper coils, each carrying current $I = 100$ A. Since deviations from the theoretical form are expected to manifest as a function of the radius from the central null toward the coils, the relaxation routine characterizes these magnetic-field-strength deviations in the immediate vicinity of the null only, as seen in Fig. 4. This is accomplished by calculating the percent difference between the theoretical B_t and conducting-coil B_c magnetic field magnitudes, via the relationship

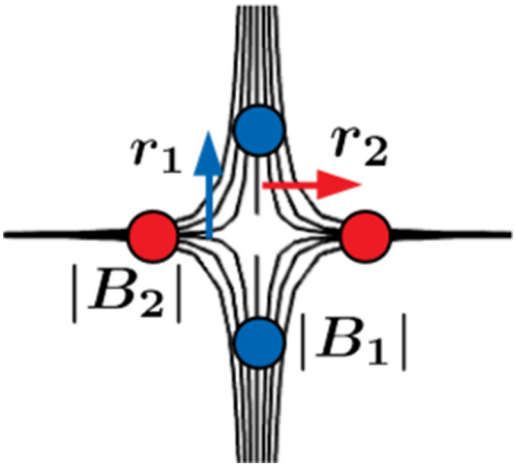

FIG. 4. A schematic of the custom magnetic null relaxation method. The magnetic field strengths B_1 and B_2 are sampled in the immediate z (r_1) and x (r_2) vicinity of the null, respectively. The magnitude of the theoretical B_0 value follows a relaxation routine to minimize the percent difference between B_1 and B_2 of order 10^{-4}%.

$$\%\ \mathrm{diff} = \frac{|B_t - B_c|}{B_t} \times 100. \quad (7)$$

The quantities r_1 and r_2 are taken at a single-pixel position in the $\pm z$ and $\pm x$ directions, respectively. Beginning with an initial guess, the quantity B_0 is constrained iteratively to match the percent differences to within 10^{-4}%. This optimal 10^{-4}% value is chosen from the empirical inspection of the resulting percent-difference maps (see Sec. III) and corresponds to a confidence interval of 5σ. Relaxation of the B_0 value follows the selection criterion

$$B_0^\star = B_0 + K(B_t - B_c)B_0, \quad (8)$$

where the sign of $(B_t - B_c)$ forces $B_0^\star$ toward convergence with the experimental field. The multiplication factor K begins at the upper limit of 100, rapidly converging B_0 to within a few percent. The supervised portion of this relaxation method comes in during the reduction of K to a value

as small as 0.01 to achieve convergence. Typical solutions are found with $K = 0.05$.

III. RESULTS

Results are presented for the test case of the theoretical magnetic field of Eq. (3) using parameters $p = 1$, $q = j_{\parallel} = j_{\perp} = 0$, characteristic length $L = 0.10$ m (10 cm), and the experimental 0.5-m radius spherical assembly of 20 copper coils ($\rho = 8.96$-g cm^{-3}, $J_e = 500$ A cm^{-2}) and current $I = 100$ A. The relaxation method determines $B_0 = 1.604\,96 \times 10^{-4}$ T to 5σ accuracy. All 3D magnetic-field-streamline visualizations are created using the open-source MAYAVI package [37].

A. Topologies of the magnetic field

Figure 5(a) shows a 3D magnetic-field-streamline image of the theoretical 3D null-point field using the above parameters. The field lines are constrained to a 1-m^3 cube with the null at the origin. Identical views of the magnetic field streamlines for the conducting-coil assembly are shown in Fig. 5(b). It can be seen that the overall fan-spine structure is replicated by the coil architecture, with the only immediate difference being the maximum magnetic field strength (see the color bars).

Significant deviations from the theoretical field will increase at radial distances approaching the coil boundaries from the central null. Therefore, we analyze the magnitude and direction of the vector magnetic field within an inner volume close to the null point. Figure 6 shows cross sections of the vector magnetic field through the null, both along the spine axis (top) and in the fan plane (bottom), for the theoretical field (left column) and the conducting-coil assembly (right column). The magnetic field is considered within the inner square of side 20 cm, centered on the null point, corresponding to an inner area of 400 cm^2. In both cases, the central null point is clearly evident, with field vectors pointing in along the fan plane and out along the spine axis, as expected by our choice of the sign of the I direction and sign of B_0. Again, in both cases, the magnetic field strengths are visually identical, with both the top and bottom views having the same color-bar scaling, respectively. The magnitude of **B** at a distance $r = L$ in the x-y plane is seen to be approximately $B_0 \approx 1.6 \times 10^{-4}$ T, as expected. If either the magnitude of the theoretical parameter B_0 or the magnitude of the coil current I are changed, the correspondence between the two fields will begin to deviate. This fact will be further clarified in Sec. III B.

B. Statistical results

Figure 7 displays the percent differences between the theoretical and coil fields, both along the spine axis (left column) and in the fan plane (right column). The top row

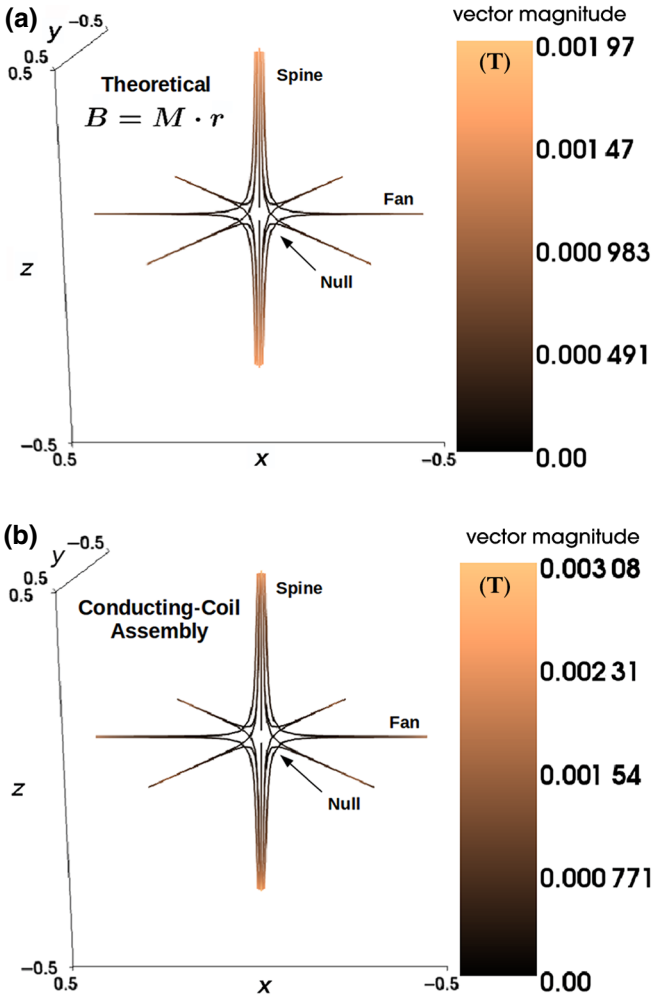

FIG. 5. (a) The streamlines of a theoretical 3D radial magnetic null point of Eq. (1) with $p = 1$, $q = j_{\parallel} = j_{\perp} = 0$, and $B_0 = 1.604\,96 \times 10^{-3}$ T. The streamlines are constrained to a radius of 0.5 m. (b) The streamlines of the spherical conducting-coil assembly of Fig. 3 with 20 coils in total, radius $|\vec{r}| = 0.5$ m, and $I = 100$ A. The color-bar units are tesla.

is the same inner 400-cm^2 area as in Fig. 6, with the bottom row enlarged to focus on the inner square with side 10 cm and area 100 cm^2. Interestingly, along the spine axis, within the inner 400 cm^2 the percent difference approaches $\lesssim$0.60%, while the inner 100-cm^2 volume does not exceed approximately 0.16%. In the fan plane, the percent errors are a bit higher, with a maximum of approximately 1.20% inside the inner 400 cm^2 and below approximately 0.25% within the inner 100 cm^2. Therefore, inside the inner null point region, which is a few centimeters across, any experimental dynamics can be diagnosed as taking place within a high-order theoretical 3D null point.

The shape of the coil assembly field deviations from the theoretical are seen to magnify as one moves out from the null either along the fan plane (radial x-y) or along the spine axis (z axis). The source of this error

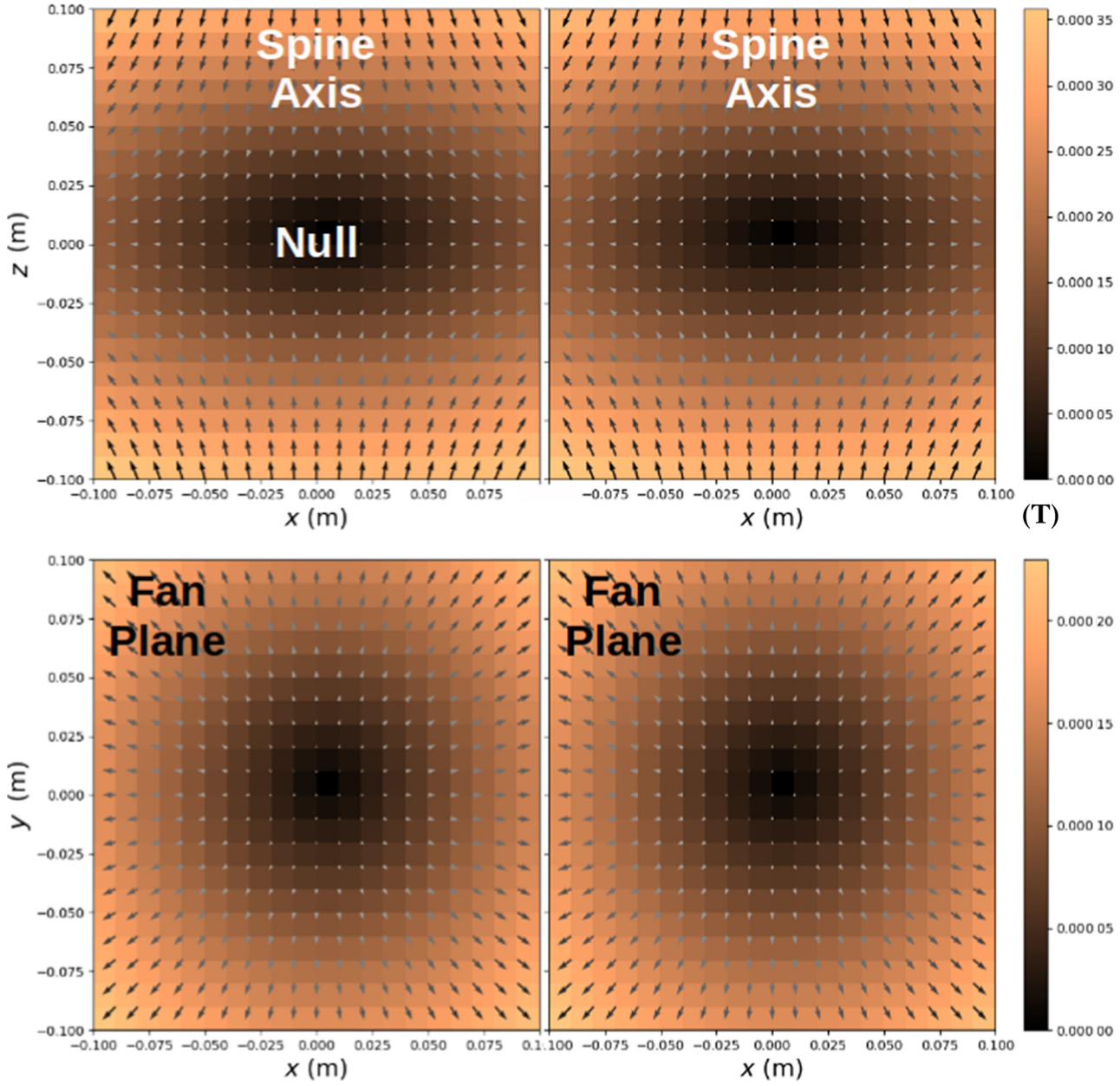

FIG. 6. Cross sections of the inner 400-cm^2-area vector magnetic flux density. The left column shows the x-z (top) and x-y (bottom) cross sections through the central null of the theoretical null point field. The right column shows identical cross sections for the conducting-coil assembly magnetic field. The arrows denote the vector-magnetic-field directions. A low-resolution grid is used to highlight the vector directions. In both cases, the $\pm z$-direction field lines point in along the spine ($x = 0$ up and down), while the vectors point out along the fan plane away from the null ($z = 0$; positive null point). The color-bar units are tesla. It can be seen that the value of $|B_0| \approx 1.6 \times 10^{-4}$ T is achieved at a radius of $r = L = 0.10$ m in the x-y plane.

seems to be the slope dB/dr by which the magnetic field of the coils increases as one moves toward the coils in these directions. Additionally, increasing the number of coils per hemisphere N, all with identical current magnitude I, will increase the magnitude of the magnetic field along the spine axis, as a function of the radius, compared with the theoretical. This effect is demonstrated in the streamlines of Fig. 5(b), where the spine magnetic field magnitude is the source of increasing deviations. Fortunately, the strengthening z-axis field magnitude acts to collimate the spine-axis field-line topology as a function of the radius (see Sec. IV), which is a shortcoming of the generalized two-coil reversed-Helmholz-coil configuration. These results justify the choice of the spherically symmetric geometry for production of the 3D null. The maximum percent errors are concentrated along the radial

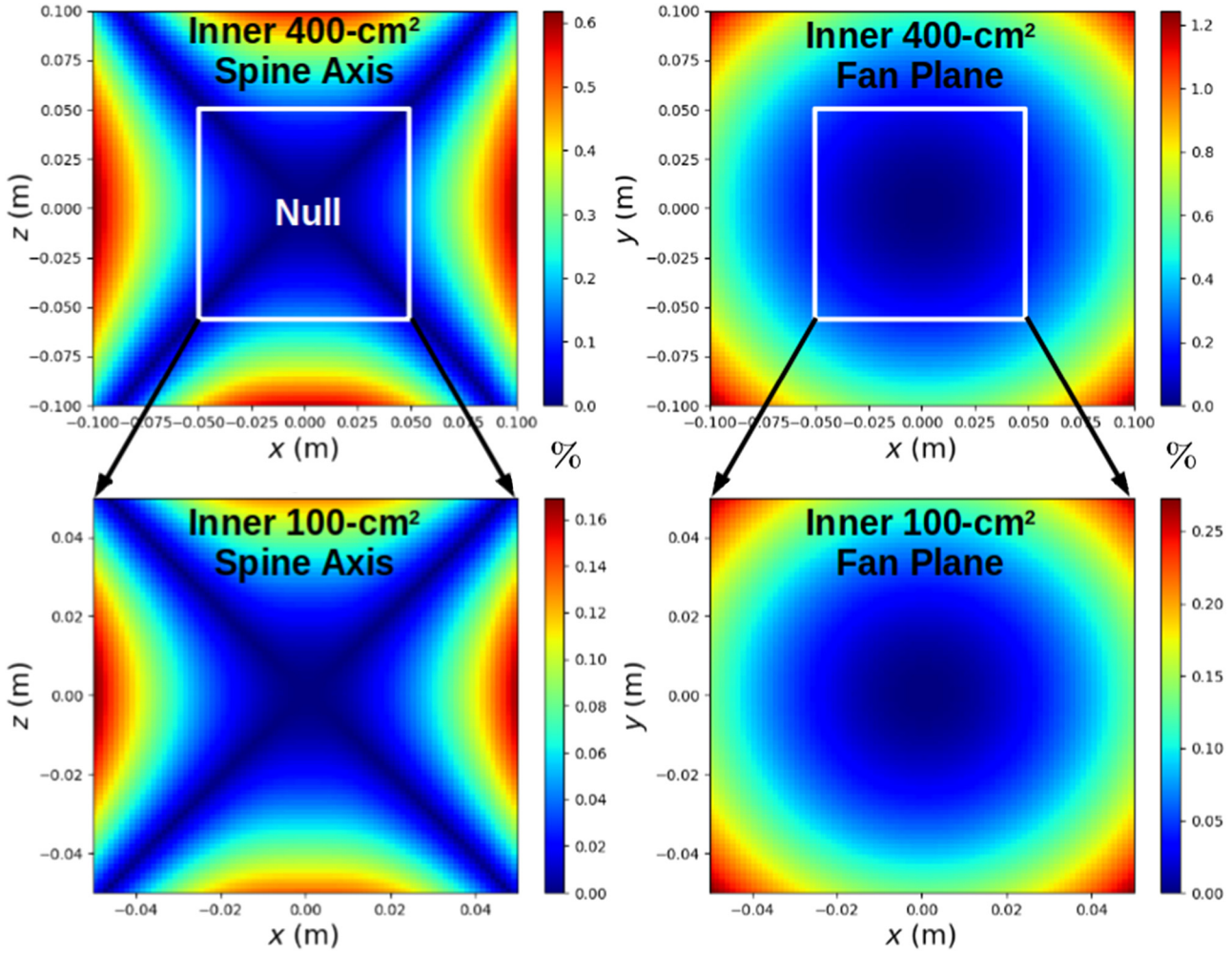

FIG. 7. The percent-difference cross sections in the x-z (left) and x-y (right) plane between the theoretical and conducting-coil assembly magnetic field magnitudes, centered on the null. The top row is the inner 400-cm^2 area (20-cm sides). The bottom row shows the corresponding inner 100-cm^2 area (10-cm sides) percent differences.

fan plane (x direction) and the spine axis (z direction), with symmetric approximately 45° "cones" of vanishing errors (blue in Fig. 7). We attempt nonspherical geometries with constant coil current I, including a solenoid and cone; however, higher percent errors become amplified along either the fan plane or the spine axis. A constant-current solenoid approaches a uniform axial field away from the null, inconsistent with the spine axis in Eq. (3), while a constant-current cone of arbitrary slope is found to amplify errors along the fan plane compared to the spine. The choice of spherical geometry in this study evenly distributes the percent error throughout the volume.

To determine the origin of the increasing errors as one moves away from the null along either the fan plane or the spine axis, we also quantify the percent differences between the theoretical and coil-assembly components B_x, B_y, and B_z. Figure 8 denotes the percent-difference cross sections for each of the Cartesian components. It is evident that the B_x and B_y components contribute the smallest error, with the B_y component along the spine axis being identically 0%. The B_z component dominates the error, which corresponds to increasing deviations from the theoretical as a function of z (see Sec. IV).

Volumetric deviations from the theoretical field as a function of the radius are quantified by integrating the percent error over concentric spheres of increasing radii. In radial increments of 0.5 cm, Fig. 9 shows both the volumetric average percent error and the volumetric maximum percent error, out to a radius of 25 cm from the central null point. It is interesting to note that the maximum percent error does not exceed 1% until a radius of approximately 13 cm, while the average percent difference stays below 1% until approximately 20 cm in radius.

We further quantify the degree of deviation from the theoretical by calculating the angle offsets θ between Eq. (3)

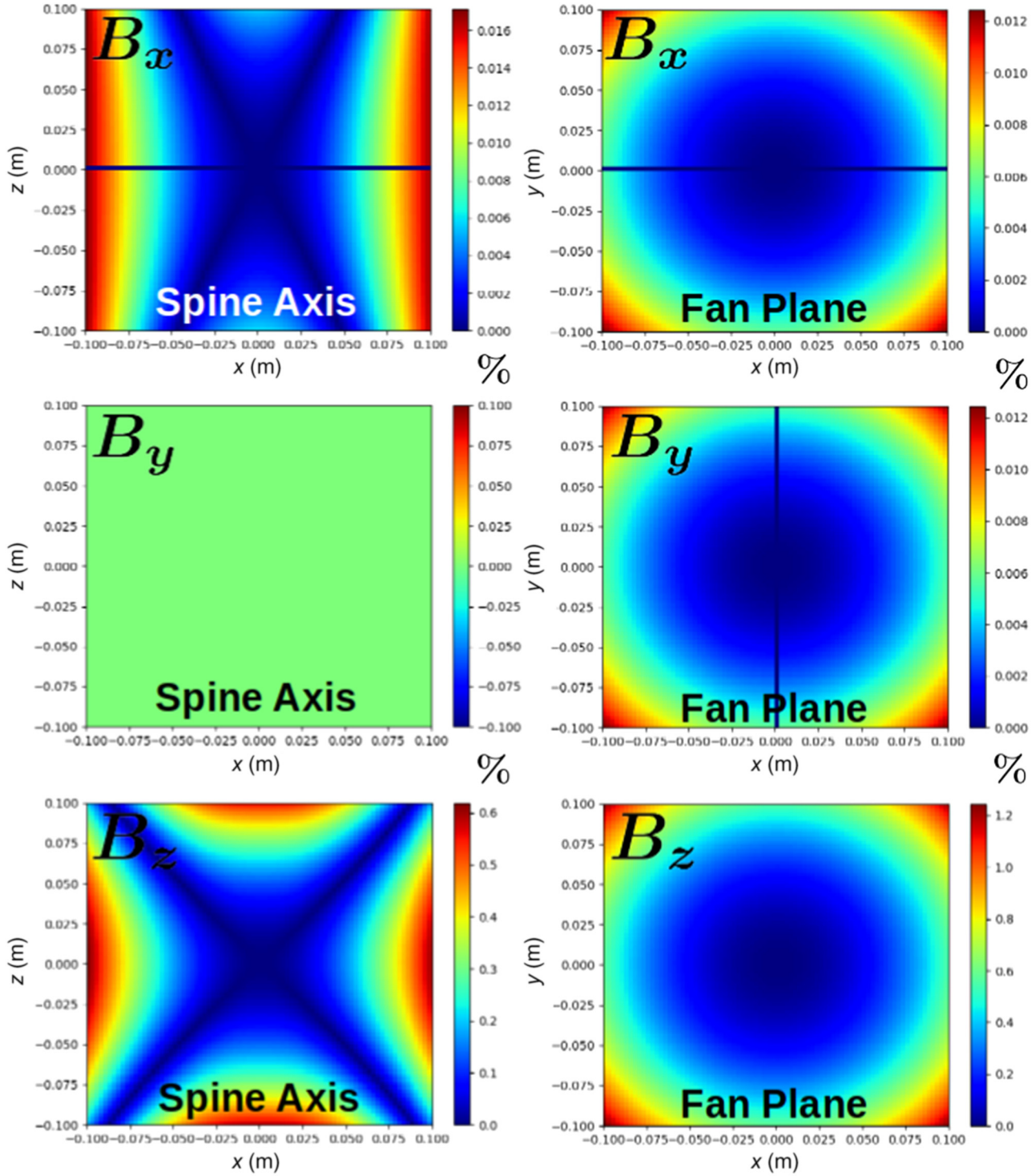

FIG. 8. The percent-difference cross sections in the x-z (left) and x-y (right) plane of the vector-component magnitudes (from top to bottom, B_x, B_y, and B_z) between the theoretical and conducting-coil assembly magnetic fields, centered on the null. Each size is the inner 400-cm^2 area (20-cm sides). The error is dominated by the B_z components.

and Eqs. (4), (5), and (6). Exploiting the relationship

$$\theta = \arccos\left(\frac{\mathbf{B_t}\cdot\mathbf{B_c}}{B_t B_c}\right), \tag{9}$$

Figure 10 denotes the offset angle (in degrees) between the theoretical and coil vector-magnetic fields. A constraint is enforced where positive (negative) offsets correspond to the coil-magnetic-field vector component being tilted

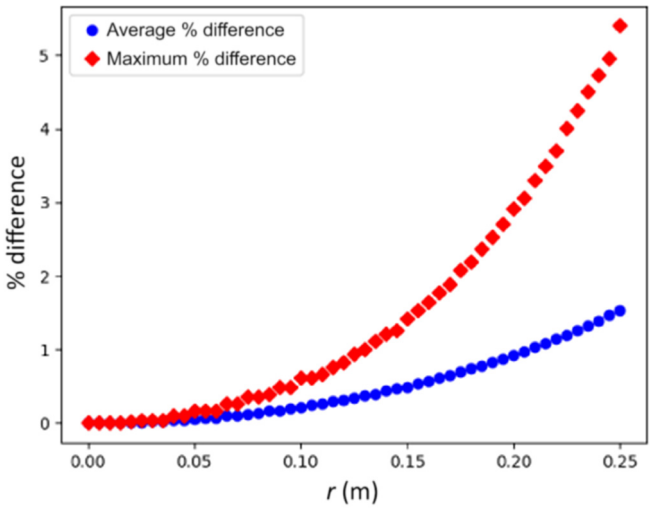

FIG. 9. The average (blue circles) and maximum (red diamonds) percent differences within concentric diagnostic spheres as a function of the radius from the null. The percent error stays below 1% out to a radius of approximately 20 cm.

toward (away from) the z axis compared to the theoretical. Figure 10 confirms the qualitative expectation that strengthening the magnetic flux density as a function of z, due to constant coil current I, corresponds to the coil-assembly magnetic field vectors tilting toward the spine axis (positive angle values). Within the inner 400 cm^2 area (20-cm sides), the angle offset is $\lesssim 0.4^\circ$ and within the central 100 cm^2 area (10-cm sides), this offset is $\lesssim 0.1^\circ$. These results demonstrate that this test-case geometry of a spherical assembly of coils can closely approximate a theoretical 3D null out to a significant radius.

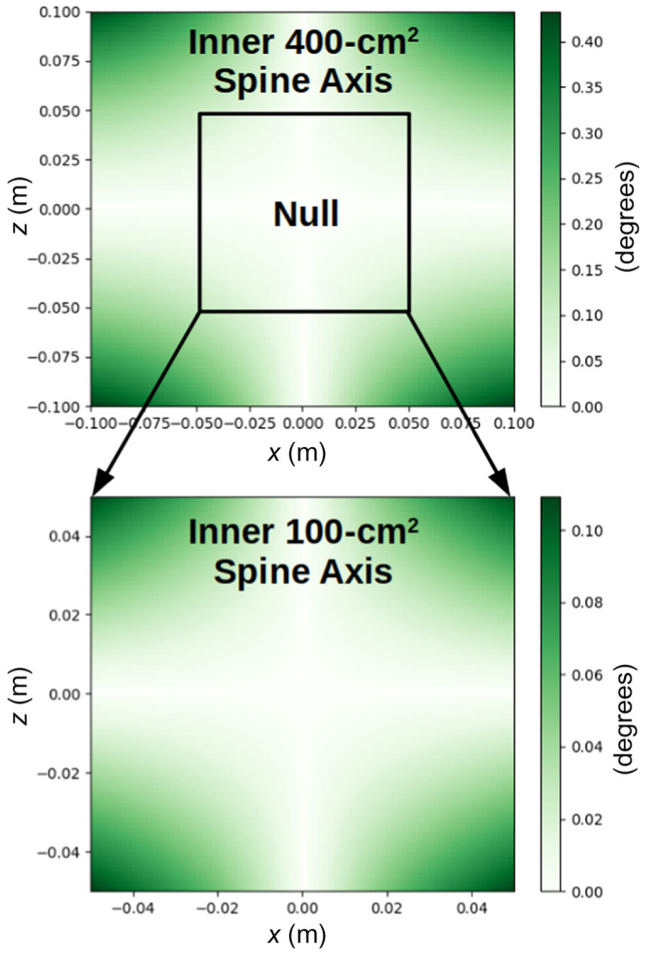

FIG. 10. Cross sections in the x-z plane of the angle-offset magnitudes between the theoretical and conducting-coil-assembly magnetic field vectors: top, the inner 400-cm^2 area; bottom, the inner 100-cm^2 area. The positive values correspond to coil field vectors pointing more toward the z axis than the theoretical. The spine axis and fan plane are precisely aligned (zero offset), with angle offsets increasing away from these axes. The color-bar units are degrees.

C. Scalability

We recognize that the presented test case is only a proof of concept with relatively low current I and characteristic B_0 magnitude. As such, we have undertaken an analysis of how this conducting coil assembly scales to higher energies. In this scalability problem of a fixed-radius spherical assembly (0.5 m), there are three independent variables: the coil current I, the magnitude of the characteristic magnetic field strength B_0, and the number of coils per hemisphere N. Our scalability analysis answers the question of how the theoretical $|B_0|$ would change with both differing current I and, independently, a differing number of coils per hemisphere N? Here, we consider the characteristic length $L = 0.10$ m as constant, to investigate the scalability of I, N, and B_0 only.

Since the magnetic field of a current-carrying coil is linearly dependent on the current (i.e., $B \propto I$) by the Biot-Savart law, an increase (or decrease) in current corresponds to a linear increase (or decrease) in the required $|B_0|$. However, due to the nature of specifying $|B_0|$ to many significant figures to match the I and N infrastructure, we empirically determine $|B_0|$ for a range of N coils per hemisphere for four separate currents, $I = [100, 200, 300, 400]$ A (Table I). The relaxation method of Sec. II D is utilized to give 10^{-4}% percent-difference minimization as in Fig. 7. The results of these empirical analyses are plotted in Fig. 11 and are inclusive of linear regression fits using SCIPY.STATS.LINREGRESS. Error bars exist below the resolution of the tick marks. These empirical relationships, each to high-order accuracy ($R_{100} \approx R_{200} \approx R_{300} \approx R_{400} \approx 0.999\,987$), demonstrate that per current value, there is both a linear increase in $|B_0|$ with respect to N depending on the slope m_I and a 1:1 linear increase in the slopes m_I with respect to the current magnitudes (i.e., double I and double $|B_0|$).

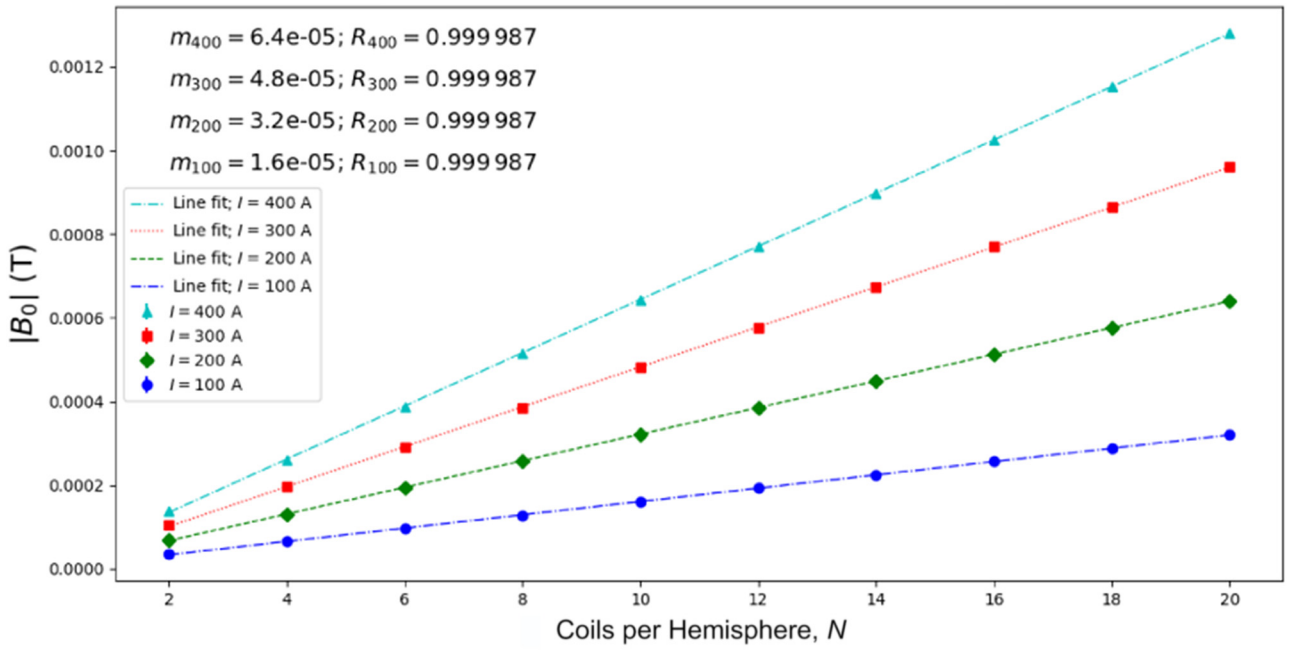

FIG. 11. The empirical linear scaling relationship between the number of coils per hemisphere N and the required theoretical characteristic magnetic field magnitude $|B_0|$. The error bars are below the resolution of the tick marks. This relationship can be used to construct radial magnetic null points of any desired size and magnitude.

Our empirically determined relationship,

$$|B_0| \approx 1.6 \times 10^{-5}\ [\mathrm{T}] \cdot N \cdot \left(\frac{I}{100\ [\mathrm{A}]}\right), \qquad (10)$$

can therefore be used to construct magnetic nulls of any desired magnitude. The slope of 1.6×10^{-5} T is limited to the 0.5-m radius of the chosen spherical assembly. Assemblies over a range of sphere radii will require analyses beyond the scope of this paper, but are expected to follow linear scaling relationships between I and N as well, but with slopes that differ from those of Eq. (10). This topic, covering a wider range of scalability, is anticipated for a forthcoming study.

IV. DISCUSSION AND CONCLUSION

We present the engineering infrastructure for a conducting-coil assembly with the ability to produce 3D magnetic null points [2,24,38] in both topology and magnitude, to fairly high order. The analytically determined spherical aggregation of circular copper coils can produce the vector magnetic field of a theoretical 3D null point [29,30] to $\lesssim$1% accuracy within a volume of 8×10^3 cm^3 and $\lesssim$0.2% accuracy within the central 1×10^3 cm^3. These volumes are sufficiently large that future experimentation, e.g., plasma studies of torsional magnetic reconnection, will have the ability to compare induced and observed dynamics about experimental 3D nulls with the results of computational models [18,21,26] that use the background potential magnetic field of the form given in Eq. (3).

A benefit of the algorithm presented here is that the conducting-coil assembly and the resulting magnetic null point field are calculated using accurate depictions of both the finite copper-coil torus size and exact magnetic field solutions outside the conductor. The results presented here demonstrate a pathway for experimenters to use in constructing spherical assemblies of coils using arbitrary conducting materials, be they nonsuperconducting or superconducting. Knowledge of a required characteristic magnetic field strength B_0 at a characteristic distance L can be applied to generate magnetic configurations of varying energies. The number of coils per hemisphere N can be optimized to carry current I such that the spatial dimensions are minimized and that adjacent coil dimensions do not overlap. While solutions for a lesser number of coils are presented in Fig. 11, a larger number of coils per hemisphere N presents the benefit of enforcing a spine axis of collimated magnetic field lines. A lower N introduces error in that the spine-axis magnetic-field-line directions diverge from the z axis, since there are no coils at the poles to collimate the spine field lines (Fig. 1).

The benefits of using Eqs. (4), (5), and (6) thus constitute a marked improvement over using the computationally expensive Biot-Savart law. However, an engineering drawback of this design is the independent dc powering of each coil. Either $2N$ power supplies or parallel powering through one power supply will be necessary. Alternatively,

series powering is possible but carries with it the drawback that any individual coil failure causes the entire assembly to fail. Other errors can arise from coil misalignment but these may be mitigated by using sufficiently strong structural material or even additive manufacturing techniques as a rigid frame for the coil assembly. Additionally, further multicoil techniques may be employed for canceling fringing magnetic fields along the fan or spine to achieve higher-purity 3D nulls. Such techniques are common in magnetic shielding studies using high-temperature superconductors [39] and may be scaled down for such an application.

We recognize that this spherical assembly of circular conducting coils is only one first-order approximation of a "pure" 3D null-point magnetic field. However, as shown in Fig. 7 the percent differences are relatively evenly distributed throughout the volume, with approximately 45° cones of vanishing error. We argue that nonspherical geometries with constant current will introduce higher errors along the fan or spine, but this analysis is beyond the scope of this paper. Other established, and perhaps proprietary, algorithms for producing multilayer helical conducting coils [32–34] may be able to make significant improvements upon the design and purity of the field presented here. This includes considerations of nonspherical geometries and of nonconstant currents. Such studies are beyond the scope of this paper but are worthwhile future works. This paper introduces a conducting-coil concept that is able to experimentally match the mathematical 3D null formulations that have been observed to be ubiquitous in a wide range of astrophysical plasma environments [1,2,4,38,40,41]. Since 3D nulls in magnetic reconnection environments are kinetic scale [1], through the utilization of such conducting-coil assemblies within a relatively low-density collisionless plasma environment where the mean free path is on the order of the scale of the device, e.g., centimeter scale, full plasma motions can be observed and diagnosed [16]. These observations can further our understanding of the dynamical observations of magnetic reconnection in the turbulent magnetosheath from Cluster [4] and the Magnetospheric Multiscale Mission [42].

The deviations of the conducting-coil assembly magnetic field from the theoretical field that are quantified in Figs. 7, 8, 9, and 10 demonstrate that impurities increase radially outward from the null in the fan plane and along the spine axis. Attempts to modulate the magnitude of the coil current I (Fig. 2) are undertaken to reduce such errors. Scaling of the current as a function of z is successful in decreasing errors along the spine axis but correspondingly increases error in the fan plane and vice versa. Therefore, we settle on the constant current magnitude presented in this paper. Again, further attempts using more sophisticated multilayered algorithms may be able to mitigate these deviations along certain directions. Specifically, the fact that the error is dominated by the B_z component is a topic for further study and improvement.

Finally, a scalability analysis is able to provide the framework for producing 3D null points at higher magnetic energy densities than the proof-of-concept test case presented here. The empirical relationships determined in Sec. III C will allow researchers to create 3D null point fields of varying coil number and strength. Numerical procedures for optimizing the total number of coils and the coil current required for high-purity fields are presented in Fig. 11. Such coil assemblies may be important for future laboratory investigations of plasma processes at magnetic nulls and even for use in particle accelerators.

ACKNOWLEDGMENTS

We thank the University of the Virgin Islands, St. Thomas, U.S. Virgin Islands.

[1] V. Olshevsky, A. Divin, E. Eriksson, S. Markidis, and G. Lapenta, Energy dissipation in magnetic null points at kinetic scales, Astrophys. J. Lett. **807**, 155 (2015).
[2] S. J. Edwards and C. E. Parnell, Null point distribution in global coronal potential field extrapolations, Solar Phys. **290**, 2055 (2015).
[3] D. I. Pontin, E. R. Priest, and K. Galsgaard, On the nature of reconnection at a solar coronal null point above a separatrix dome, Astrophys. J. Lett. **774**, 154 (2013).
[4] D. E. Wendel and M. L. Adrian, Current structure and nonideal behavior at magnetic null points in the turbulent magnetosheath, J. Geophys. Res. (Space Phys.) **118**, 1571 (2013).
[5] R. Albanese and the DTT Project Proposal Contributors, DTT: A divertor tokamak test facility for the study of the power exhaust issues in view of DEMO, Nucl. Fus. **57**, 016010 (2017).
[6] M. Inomoto, T. G. Watanabe, K. Gi, K. Yamasaki, S. Kamio, R. Imazawa, T. Yamada, X. Guo, T. Ushiki, H. Ishikawa, H. Nakamata, N. Kawakami, T. Sugawara, K. Matsuyama, K. Noma, A. Kuwahata, and H. Tanabe, Centre-solenoid-free merging start-up of spherical tokamak plasmas in UTST, Nucl. Fus. **55**, 033013 (2015).
[7] J. Egedal, W. Fox, N. Katz, M. Porkolab, K. Reim, and E. Zhang, Laboratory Observations of Spontaneous Magnetic Reconnection, Phys. Rev. Lett. **98**, 015003 (2007).
[8] R. L. Stenzel, J. M. Urrutia, M. Griskey, and K. Strohmaier, A new laboratory experiment on magnetic reconnection, Phys. Plasmas **9**, 1925 (2002).
[9] J. Egedal, A. Fasoli, M. Porkolab, and D. Tarkowski, Plasma generation and confinement in a toroidal magnetic cusp, Rev. Sci. Instrum. **71**, 3351 (2000).
[10] M. Yamada, H. Ji, S. Hsu, T. Carter, R. Kulsrud, N. Bretz, F. Jobes, Y. Ono, and F. Perkins, Study of driven magnetic reconnection in a laboratory plasma, Phys. Plasmas **4**, 1936 (1997).

[11] R. A. Lane and C. A. Ordonez, Classical trajectory Monte Carlo simulations of particle confinement using dual levitated coils, AIP Adv. **4**, 077117 (2014).
[12] E. Thomas, Jr., R. L. Merlino, and M. Rosenberg, Magnetized dusty plasmas: The next frontier for complex plasma research, Plasma Phys. Controlled Fus. **54**, 124034 (2012).
[13] N. Nishizuka, Y. Hayashi, H. Tanabe, A. Kuwahata, Y. Kaminou, Y. Ono, M. Inomoto, and T. Shimizu, A laboratory experiment of magnetic reconnection: Outflows, heating, and waves in chromospheric jets, Astrophys. J. Lett. **756**, 152 (2012).
[14] T. W. Kornack, P. K. Sollins, and M. R. Brown, Experimental observation of correlated magnetic reconnection and Alfvénic ion jets, Phys. Rev. E **58**, R36 (1998).
[15] M. Yamada, H. Ji, S. Hsu, T. Carter, R. Kulsrud, Y. Ono, and F. Perkins, Identification of Y-Shaped and O-Shaped Diffusion Regions during Magnetic Reconnection in a Laboratory Plasma, Phys. Rev. Lett. **78**, 3117 (1997).
[16] D. L. Chesny, N. B. Orange, H. M. Oluseyi, and D. R. Valletta, Toward laboratory torsional spine magnetic reconnection, J. Plasma Phys. **83**, 905830602 (2017).
[17] D. L. Chesny and N. B. Orange, Method and apparatus for torsional magnetic reconnection, U.S. Patent No. 62/664,968 (2018).
[18] J. O. Thurgood, D. I. Pontin, and J. A. McLaughlin, Three-dimensional oscillatory magnetic reconnection, Astrophys. J. Lett. **844**, 2 (2017).
[19] A. Gascoyne, Dynamics of charged particle motion in the vicinity of three dimensional magnetic null points: Energization and chaos, Phys. Plasmas **22**, 032907 (2015).
[20] D. I. Pontin, Theory of magnetic reconnection in solar and astrophysical plasmas, Philos. Trans. R. Soc. Lond. Ser. A **370**, 3169 (2012).
[21] D. I. Pontin, A. K. Al-Hachami, and K. Galsgaard, Generalised models for torsional spine and fan magnetic reconnection, Astron. Astrophys. **533**, A78 (2011).
[22] D. I. Pontin, Three-dimensional magnetic reconnection regimes: A review, Adv. Space Res. **47**, 1508 (2011).
[23] P. Wyper and R. Jain, Torsional magnetic reconnection at three dimensional null points: A phenomenological study, Phys. Plasmas **17**, 092902 (2010).
[24] E. R. Priest and D. I. Pontin, Three-dimensional null point reconnection regimes, Phys. Plasmas **16**, 122101 (2009).
[25] S. Dalla and P. K. Browning, Particle trajectories and acceleration during 3D fan reconnection, Astron. Astrophys. **491**, 289 (2008).
[26] D. I. Pontin and K. Galsgaard, Current amplification and magnetic reconnection at a three-dimensional null point: Physical characteristics, J. Geophys. Res. (Space Phys.) **112**, A03103 (2007).
[27] S. Dalla and P. K. Browning, Jets of energetic particles generated by magnetic reconnection at a three-dimensional magnetic null, Astrophys. J. Lett. **640**, L99 (2006).
[28] S. Dalla and P. K. Browning, Particle acceleration at a three-dimensional reconnection site in the solar corona, Astron. Astrophys. **436**, 1103 (2005).
[29] C. E. Parnell, T. Neukirch, J. M. Smith, and E. R. Priest, Structure and collapse of three-dimensional magnetic neutral points, Geophys. Astrophys. Fluid Dyn. **84**, 245 (1997).
[30] C. E. Parnell, J. M. Smith, T. Neukirch, and E. R. Priest, The structure of three-dimensional magnetic neutral points, Phys. Plasmas **3**, 759 (1996).
[31] S. Fukao, M. Ugai, and T. Tsuda, Topological study of magnetic field near a neutral point, Rep. Ionosphere Space Res. Jpn. **29**, 133 (1975), **29**, 133 (1975).
[32] C. Goodzeit, R. Meinke, and M. Ball, Concentric tilted double-helix dipoles and higher-order multipole magnets, U.S. Patent No. 6921042 B1, 10/067, 487 (2005).
[33] S. S. Chouhan, M. A. Green, and A. F. Zeller, Iron dominated mixed multipole magnets with conventional or superconducting coils, IEEE Trans. Appl. Supercond. **24**, 1 (2014).
[34] V. Kashikhin, A novel design of iron dominated superconducting multipole magnets with circular coils, IEEE Trans. Appl. Supercond. **20**, 196 (2010).
[35] D. I. Pontin, G. Hornig, and E. R. Priest, Kinematic reconnection at a magnetic null point: Spine-aligned current, Geophys. Astrophys. Fluid Dyn. **98**, 407 (2004).
[36] J. Simpson, J. Lane, C. Immer, and R. Youngquist, in *Simple Analytic Expressions for the Magnetic Field of a Circular Current Loop* (IEEE Transactions on Magnetics, 2001), p. 1.
[37] P. Ramachandran and G. Varoquaux, MAYAVI: 3D visualization of scientific data, Comput. Sci. Eng. **13**, 40 (2011).
[38] M. S. Freed, D. W. Longcope, and D. E. McKenzie, Three-year global survey of coronal null points from potential-field-source-surface (PFSS) modeling and Solar Dynamics Observatory (SDO) observations, Solar Phys. **290**, 467 (2015).
[39] L. Wéra, J. F. Fagnard, G. A. Levin, B. Vanderheyden, and P. Vanderbemden, Magnetic shielding with YBCO coated conductors: Influence of the geometry on its performances, IEEE Trans. Appl. Supercond. **23**, 8200504 (2013).
[40] E. I. Mason, S. K. Antiochos, and N. M. Viall, Observations of solar coronal rain in null point topologies, Astrophys. J. Lett. **874**, L33 (2019).
[41] M. Janvier, Three-dimensional magnetic reconnection and its application to solar flares, J. Plasma Phys. **83**, 535830101 (2017).
[42] W. M. Macek, M. V. D. Silveira, D. G. Sibeck, B. L. Giles, and J. L. Burch, Mechanism of reconnection on kinetic scales based on Magnetospheric Multiscale Mission observations, Astrophys. J. Lett. **885**, L26 (2019).